On the convergence of the modified elastic-viscous-plastic method for solving the sea ice momentum equation

Madlen Kimmritz[a,*], Sergey Danilov[a,b], Martin Losch[a]

[a] Alfred Wegener Institute, Bussestrasse 24, D-27570 Bremerhaven
[b] A. M. Obukhov Institute of Atmospheric Physics RAS, Moscow, Russia

Abstract

Most dynamic sea ice models for climate type simulations are based on the viscous-plastic (VP) rheology. The resulting stiff system of partial differential equations for ice velocity is either solved implicitly at great computational cost, or explicitly with added pseudo-elasticity (elastic-viscous-plastic, EVP). A recent modification of the EVP approach seeks to improve the convergence of the EVP method by re-interpreting it as a pseudotime VP solver. The question of convergence of this modified EVP method is revisited here and it is shown that convergence is reached provided the stability requirements are satisfied and the number of pseudotime iterations is sufficiently high. Only in this limit, the VP and the modified EVP solvers converge to the same solution. Related questions of the impact of mesh resolution and incomplete convergence are also addressed.

Keywords: Viscous-plastic rheology, Elastic-viscous-plastic rheology, Sea ice, FESOM

2010 MSC: 00-01, 99-00

1. Introduction

The basis of most current sea-ice models is the assumption of viscous-plastic (VP) rheology connecting the ice deformation rates with stresses in the ice [1]. The resulting set of equations is very stiff due to the non-linearity in the VP rheology. Hence, they are computationally challenging and require efficient solution

*Corresponding author

Email addresses: madlen.kimmritz@awi.de (Madlen Kimmritz), sergey.danilov@awi.de (Sergey Danilov), martin.losch@awi.de (Martin Losch)

methods to avoid the restriction to very small time steps in standard explicit methods. Partial linearisation allows the stiff part of the problem to be treated implicitly [2]; this requires using solvers but lifts the time step limitation. However, because of linearisation, that is, splitting the operator into implicit and explicit parts and estimating viscosity using the previous Picard iterate, far too many (Picard) iterations ($O(10^4)$) are required to achieve method convergence, so that traditionally only a few iterations are made and convergence is sacrificed [3]. This motivated the implementation of fully nonlinear Jacobian-free Newton-Krylov (JFNK) solvers [4, 5, 6]. They converge faster but still remain an expensive solution.

The elastic-viscous-plastic (EVP) method is an alternative to implicit methods. It relaxes the time step limitation of the explicit VP method by introducing an additional elastic term to the stress equations. This allows a fully explicit implementation with much larger time steps than for the explicit VP method [7, 8] but requires subcycling within the external time step set by the ocean model. The effects of the additional elasticity term, however, are reported to lead to noticeable differences in the deformation field, and to lead to smaller viscosities and weaker ice [e.g., 5, 9, 10, 11]. In many cases these effects are linked to the violation of stability limits (analogous to the CFL-criterion for advection) associated with the explicit time stepping scheme of the subcycling process [7, 8]. Their most frequent manifestation is grid-scale noise in the ice divergence field and hence in viscosities. While the numerical code as a rule remains stable and maintains smooth distributions of ice concentration and thickness, the noise in the ice velocity divergence may deteriorate solutions, in particular on meshes with fine or variable resolution [10]. In an effort to improve the performance of the EVP method, a modification of the time-discrete EVP model (EVP*) was proposed by adding an inertial time stepping term to the momentum balance [5]. This EVP* method was further reformulated by [11] as a “pseudotime” iterative scheme converging to the VP rheology. By construction, it should lead to solutions identical to those of the VP method provided it converges and remains stable. Yet, despite improvements in solutions, the convergence has not been achieved [11].

Here we reconsider the elementary analysis of stability of the EVP* method carried out by [11] and conduct a series of numerical simulations that are aimed at clarifying conditions under which the convergence can be achieved. This is the main question that we address in this paper. Additionally, we are going to illustrate the implications of our findings as the resolution is refined. We also explore the consequences of incomplete convergence (limited by the prescribed number of pseudotime steps) on the quality of the EVP* solution.

We start with an introduction of the EVP* scheme as formulated in [11] and elaborate on the convergence conditions of a simplified one-dimensional (1D) scheme. Although this analysis largely follows that by [11], we arrive at new conclusions that help to formulate an optimal strategy. Subsequently, we discuss our results on the basis of experiments performed with the unstructured-mesh finite-element sea ice model FESIM [12], which is a component of the Finite-Element Sea ice–Ocean Model FESOM [13]. Finally, conclusions and outlook are presented.

2. The EVP* method

The horizontal momentum balance of sea ice is written as

$$m(\partial_t + \mathbf{f}\times)\mathbf{u} = a\boldsymbol{\tau} - C_d a \rho_o (\mathbf{u} - \mathbf{u}_o)|\mathbf{u} - \mathbf{u}_o| + \mathbf{F} - mg\nabla H. \tag{1}$$

Here m is the ice (plus snow) mass per unit area, $\mathbf{f}$ is the Coriolis vector, a the ice compactness, $\mathbf{u}$ and $\mathbf{u}_o$ the ice and ocean velocities, ρ_o is the ocean water density, $\boldsymbol{\tau}$ the wind stress, H the sea surface elevation, g the acceleration due to gravity and $F_j = \partial\sigma_{ij}/\partial x_i$ the contribution from stresses within the ice. We follow [11] in writing the VP constitutive law as

$$\sigma_{ij}(\mathbf{u}) = \frac{P}{2(\Delta + \Delta_{\min})}[(\dot\epsilon_{kk} - \Delta)\delta_{ij} + \frac{1}{e^2}(2\dot\epsilon_{ij} - \dot\epsilon_{kk}\delta_{ij})], \tag{2}$$

where

$$\dot{\epsilon}_{ij} = \frac{1}{2}(\partial_i u_j + \partial_j u_i), \quad \text{and} \quad \Delta = \left(\dot{\epsilon}_d^2 + \frac{1}{e^2}\dot{\epsilon}_s^2\right)^{1/2}.$$

The parameter $e = 2$ is the ratio of the major axes of the elliptic yield curve, $\dot{\epsilon}_d = \dot{\epsilon}_{kk}$ is the divergence, and $\dot{\epsilon}_s = ((\dot{\epsilon}_{11} - \dot{\epsilon}_{22})^2 + 4\dot{\epsilon}_{12}^2)^{1/2}$ is the shear. Note that we use the replacement pressure, $(\Delta/(\Delta+\Delta_{\min}))P$, [14] in the formulation of the VP constitutive law to ensure that the stress is on elliptic yield curve when $\Delta \lesssim \Delta_{\min}$. The ice strength P is parameterized as $P = hP^* e^{-c(1-a)}$, where h is the mean thickness, and the constants P^* and c are set to $P^* = 27500$ Nm^{-2} and $c = 20$.

As mentioned above, the difficulty in the integration of (1) is the stiff character of the stress term, which requires prohibitively small time steps in an explicit time stepping scheme. The traditional approach is either implicit [2], where viscosities are estimated at the previous iteration and several iterations are made, or EVP ([7], [15]), which reduces the time step limitations by adding pseudo-elasticity. Discussion of the convergence issues can be found, for example, in [11] and is not repeated here.

The suggestion by [11] is equivalent, up to detail of treating the Coriolis and ice-ocean drag terms, to formulating the EVP* method as:

$$\sigma_{ij}^{p+1} = \sigma_{ij}^p + \frac{1}{\alpha}\Big(\sigma_{ij}(\mathbf{u}^p) - \sigma_{ij}^p\Big), \tag{3}$$

$$\mathbf{u}^{p+1} = \mathbf{u}^p + \frac{1}{\beta}\Big(\frac{\Delta t}{m}\nabla\cdot\boldsymbol{\sigma}^{p+1} + \frac{\Delta t}{m}\mathbf{R}^{p+1/2} + \mathbf{u}_n - \mathbf{u}^p\Big). \tag{4}$$

In (4), $\mathbf{R}$ sums all the terms in the momentum equation except for the rheology and the time derivative, Δt is the time step of the ice model, the index n labels the time levels, that is, discrete moments in the real time, and the index p is that of pseudotime (subcycling step number). The Coriolis term in $\mathbf{R}^{p+1/2}$ is treated implicitly in our implementation and the ice-ocean stress term is linearly-implicit $(C_d\rho_o|\mathbf{u}_o - \mathbf{u}^p|(\mathbf{u}_o - \mathbf{u}^{p+1}))$. In (3), $\sigma_{ij}(\mathbf{u}^p)$ implies that the stresses are estimated by (2) based on the velocity from iteration p, and σ_{ij}^p is the variable of the pseudotime iteration. The parameters α and β in the last formulae are large numbers that are selected from stability considerations [11]. They replace the terms $2T/\Delta t_e$ and $(\beta^*/m)(\Delta t/\Delta t_e)$, where T is the elastic damping time scale and Δt_e the subcycling time step of the standard EVP formulation, and parameter β^* has been introduced in [5]. After convergence of (3) and (4), the pseudotime terms drop out and the resulting solution is exactly the VP solution:

$$\frac{m}{\Delta t}\Big(\mathbf{u}_{n+1} - \mathbf{u}_n\Big) = \nabla \cdot \boldsymbol{\sigma}(\mathbf{u}_{n+1}) + \mathbf{R}^*, \tag{5}$$

with $\mathbf{R}^* := \lim_{p\to\infty} \mathbf{R}^{p+1/2}$ and $\mathbf{u}_{n+1} := \lim_{p\to\infty} \mathbf{u}^p$. We denote the number of iterations N over p needed to reach this limit within prescribed tolerance as N_c. If the scheme does not converge to the VP solution we set $N_c = \infty$. The new velocity $\mathbf{u}_{n+1}$ of the next time level is then given by the velocity estimated at the last pseudotime step $\mathbf{u}^N$. Initial values for $p = 1$ are taken from the previous time level n.

Note that the EVP* scheme as formulated above differs from the standard EVP in three aspects: (i) the decay rate is the same for all stress components, (ii) there is damping in the momentum equation and (iii) the time derivative in the momentum equation (the last two terms in parentheses in (4)) are estimated over the external time step Δt instead of the subcycling one. These are rather subtle differences of which (i) contributes most favourably to convergence according to our experience.

3. Analysis of the EVP* method

We reconsider the elementary stability analysis of [11]. As a prototype we analyse the following 1D simplification

$$\sigma^{p+1} = \sigma^p + \frac{1}{\alpha}\Big(\frac{P}{2\Delta^p}\partial_x u^p - \sigma^p\Big), \tag{6}$$

$$u^{p+1} = u^p + \frac{1}{\beta}\Big(\frac{\Delta t}{m}\partial_x \sigma^{p+1} + \tau\frac{\Delta t}{m} + u_n - u^p\Big)\,. \tag{7}$$

Equations (6) and (7) can be understood as modelling the behaviour of 1D perturbations with respect to a smooth quasi-equilibrium state characterized by non-zero strain rates and, hence, non-zero Δ. We assume $P/(2\Delta^p)$ to be constant for this analysis. Thus, the 1D version of (3) and (4) would formally lead to similar prototype equations in the limit of the viscous regime $\Delta \ll \Delta_{\min}$.

Following [11], we consider the homogeneous problem, that is, we neglect the forcing terms $\tau\Delta t/m$ and u_n. In contrast to the analysis in [11] we take into account the u^p term in the parentheses of (7). Keeping this term puts α and β on equal footing and leads to a different view on the numerical behaviour of the EVP* method. Eliminating σ^{p+1} in (7) we get

$$u^{p+1} - 2u^p + u^{p-1} + \left(\frac{1}{\alpha} + \frac{1}{\beta}\right)\left(u^p - u^{p-1}\right) + \frac{1}{\alpha\beta}u^{p-1} + \frac{\gamma}{\alpha\beta}u^p = 0\,. \tag{8}$$

Here $\gamma = k^2 P \Delta t/(2\Delta^p m)$ and $-k^2$ is the eigenvalue of the operator ∂_{xx}, $k^2 \leq \pi^2/\Delta x^2$.

To analyse the stability of pseudotime iterations we introduce the amplification factor $\lambda = u^{p+1}/u^p$. Equation (8) then becomes

$$(\lambda^2 - 2\lambda + 1) + \left(\frac{1}{\alpha} + \frac{1}{\beta}\right)(\lambda - 1) + \frac{1}{\alpha\beta} + \frac{\gamma}{\alpha\beta}\lambda = 0\,, \tag{9}$$

where the first term represents the numerical second derivative of u and the second term the numerical first derivative and the remaining terms correspond to zero order derivatives. As usual, the system is stable if $|\lambda| \leq 1$. Because of $\alpha, \beta \ll 1$ we can simplify equation (9) as

$$\lambda^2 - q \cdot \lambda + 1 = 0 \tag{10}$$

with $q = 2 - \gamma/\alpha\beta$, where $\gamma/(\alpha\beta)$ is kept because it is not necessarily small. It can be shown that a stable (and slightly damped) solution of (9) corresponds to the stability limit $|\lambda| = 1$ of the simplified equation. Solutions of this equation are $\lambda_{1,2} = (q \pm \sqrt{q^2 - 4})/2$. Except for $|q| \leq 2$, one of these roots always has a modulus larger than one, which leads to the formal stability condition $0 < \gamma/(\alpha\beta) < 4$.

As $|\lambda| = 1$ for any λ in the stability range, we can write $\lambda = e^{-i\omega}$ with nondimensional frequency ω. Thus, stable solutions of the simplified equations correspond to oscillatory behaviour in the pseudotime subcycling. Recalling that $\lambda_{1,2} = (q \pm \sqrt{q^2 - 4})/2$, the frequency ω is small if q is close to 2, which corresponds to $\gamma/(\alpha\beta) \ll 1$, but approaches $\pm\pi$ for q close to -2, which corresponds to values of $\gamma/(\alpha\beta)$ close to 4. This upper *linear* stability limit implies a sign change in each pseudotime step and convergence will be unlikely for the original equations, which are essentially nonlinear. We further argue that regimes with $\gamma/(\alpha\beta) \gtrsim 1$ should be avoided, because oscillations will be too fast to be properly "resolved" by the pseudotime stepping.

Assuming that frequencies are small, we can describe such oscillations directly by examination of equation (9) and without considering the approximated equation (10). Expanding λ in series of lowest admissible order (i.e. 2nd order approximation for representatives of 2nd order derivatives, etc.) we obtain

$$\omega^2 + \left(\frac{1}{\alpha} + \frac{1}{\beta}\right) i\omega - \frac{1}{\alpha\beta} - \frac{\gamma}{\alpha\beta} = 0\,. \tag{11}$$

The roots of equation (11) are

$$\omega_{1,2} = -\frac{1}{2} i \left(\frac{1}{\alpha} + \frac{1}{\beta}\right) \pm \left(-\frac{1}{4}\left(\frac{1}{\alpha} - \frac{1}{\beta}\right)^2 + \frac{\gamma}{\alpha\beta}\right)^{1/2}\,. \tag{12}$$

In the limit of weak ice (small γ) we can neglect $\gamma/(\alpha\beta)$, leading to purely imaginary $\omega_1 = -i/\alpha$ and $\omega_2 = -i/\beta$. Thus, perturbations are damped with decay rates of $1/\alpha$ for (6) and $1/\beta$ for (7). We infer that α and β should be similar for similar convergence of (6) and (7), and that the number of iterations should be several times larger than $\max\{\alpha, \beta\}$ in order to reach it. Generally, $\omega_{1,2}$ are complex-valued and oscillations are superimposed on the decay. There are no oscillations for $Re(\omega) = 0$, that is

$$\frac{\gamma}{\alpha\beta} \le \frac{1}{4}\left(\frac{1}{\alpha} - \frac{1}{\beta}\right)^2\,. \tag{13}$$

This condition is symmetric with respect to α and β. Choosing $\alpha/\beta \gg \gamma$ or

$\beta/\alpha \gg \gamma$ for large α, β formally eliminates oscillations. This is consistent with [11], but with the difference that now both parameters play the same role.

There is no need in making α and β substantially different. On the contrary, in two dimensions the vectors $\nabla \cdot \boldsymbol{\sigma}$ and $\mathbf{u}$ need not be collinear. In this case the component of $\mathbf{u}$ orthogonal to $\nabla \cdot \boldsymbol{\sigma}$ will not be affected by the update of $\boldsymbol{\sigma}$ in the subcycling, but its convergence will be defined solely by β. Moreover, as the decay rates of the perturbations in weak ice regions are $1/\alpha$ and $1/\beta$, convergence in these regions is optimal when α and β are similar. Since these parameters can be on the order of several hundred in practice, the right hand side of condition (13) is very small or even equals to zero when $\alpha = \beta$. This condition is therefore much more limiting and difficult to achieve than the weaker constraint $\gamma/(\alpha\beta) \ll 1$, which now follows from (12) if the second term in the square root term dominates. Summarizing, slow decaying oscillations should be allowed, which corresponds to the parameter range

$$\gamma/(\alpha\beta) \ll 1, \tag{14}$$

and the parameters α and β should be of similar size ($\alpha \sim \beta$).

Since γ may be large ($\gamma \approx 5 \times 10^4$ for a mesh with 10 km resolution, a time step of 1 h, ice thickness of 1 m, $\Delta = 10^{-7}$ s^{-1} and P^* of 3×10^4 Nm^{-2}), maintaining stability requires a sufficiently large product $\alpha\beta$ so that both parameters should be about several hundred. Convergence in oscillatory regimes requires the number of iterations N to be several times $2(1/\alpha + 1/\beta)^{-1}$.

Our considerations also agree with the results of Exp1-Exp4 in [11] (their Table 2 and Fig. 4): Exp1 and Exp3 converge smoothly as the product $\alpha\beta$ is sufficiently large, but do not reach convergence because $N = 300$ is by far insufficient for the selected values of $\beta = 3000$ and 947. Exp. 2 and 4 show a much faster initial convergence rate due to smaller values of β, and later on develop uncontrolled oscillations as the product $\alpha\beta$ is not sufficiently large to guarantee stability.

We stress that the above analysis is based on simplified equations, so that its implications should be interpreted at a qualitative level. In summary, in order to achieve both stability and convergence one has to take sufficiently large $\alpha \sim \beta$, and N much larger than any of them. The condition $\alpha\beta \gg \gamma$ should be considered as a rule of thumb. The quantity γ scales with the mesh size as $1/\Delta x^2$ for fixed Δt. If Δt itself varies as Δx, the scaling becomes $1/\Delta x$. The implications for $\alpha\beta$ as the mesh is refined are then straightforward.

4. Numerical experiments

In this section we demonstrate experimentally (i) that the EVP* method converges, and (ii) that the convergence depends on the selection of the parameters α and β. We further examine the effect of spatial resolution and implications of using N that is smaller than needed for convergence. The experiments presented below are carried out with the finite-element sea ice model which is a component of FESOM [12, 16]. FESOM is an A-grid model with the velocity and scalar degrees of freedom collocated at the vertices of the computational mesh, and linear representation of velocity and scalar quantities on triangles. In this case all velocity derivatives and, hence, strain rates and stresses, as well as Δ are elementwise constant, which facilitates the computations implied by (3). The divergence of stresses in the momentum equation is computed following the finite-element method through projection on test functions and integration by parts. The VP solver uses linearised equations and iteratively solves those with a biconjugate gradient stabilized (BiCGSTAB) method. The time stepping implementation follows the idea of [2]. Scalar quantities (ice and snow thicknesses and concentration) are advected by a flux-corrected transport (FCT) scheme [17].

4.1. Experimental setup

Following [8] we consider a uniform and regular triangulation of the domain $[0\,°, 10\,°] \times [30\,°, 40\,°]$ in spherical coordinates with the bottom left (south-west) corner at $(x_{\min},\, y_{\min}) = (0°, 30°)$. Ice is driven by the ocean with the velocity (in m/s)

$$u_o = 0.1(2y - y_{\min})/L_y, \quad v_o = -0.1(2x - x_{\min})/L_x,$$

with domain lengths $L_x = L_y = 10\,^\circ$. Wind stress forcing is computed as

$$\boldsymbol{\tau} = C_a \rho_a \mathbf{u}_a |\mathbf{u}_a|,$$

with $C_a = 0.00225$. Here ρ_a is the air density and the wind velocity $\mathbf{u}_a$ (in m/s) is taken as

$$u_a = 5 + (\sin(2\pi t/T) - 3)\sin(2\pi x/L_x)\sin(\pi y/L_y),$$
$$v_a = 5 + (\sin(2\pi t/T) - 3)\sin(2\pi y/L_y)\sin(\pi x/L_x),$$

with $T = 4$ days. The initial ice thickness h is 2 m, initial ice compactness increases linearly from 0 in the west to 1 in the east. In this configuration, the wind pushes the ice into the northeast corner. In our simulations the ice transport is switched on, so ice gradually piles up in the corner until it becomes sufficiently thick to be virtually stopped. Simulations show that a small regularization parameter $\Delta_{\min}$ requires large values for α and β, which immediately implies slow convergence; for this reason we use the common choice $\Delta_{\min} = 2 \cdot 10^{-9}$ s^{-1} [1].

4.2. Impact of α and β

In our first experimental set up we use a spatial resolution of $1\,^\circ$ and a time step of 3600 s. In order to get a first impression of the impact of α's and β's magnitude, we begin with the case $\alpha = \beta$ for different choices of α. Table 1 lists N_c, i.e. the numbers of substeps N which are needed to reach convergence. The convergence is measured by the Euclidian norms of the residuals of the stress and momentum equations $e_\sigma(p) := \alpha(\sum_c(\sigma_c^{p+1} - \sigma_c^p)^2)^{1/2}$ and $e_u(p) := \beta(\sum_i |\mathbf{u}_i^{p+1} - \mathbf{u}_i^p|^2)^{1/2}$, where summation is over cells c and vertices i. After convergence, the solution of the EVP* scheme satisfies the equations of the VP method, so it should be converged to the VP solution. To be specific, we will assume convergence when the residuals decayed by 10^{-12}. Figure 1 depicts the development of e_σ and e_u at time levels 1 and 144 (6 days). Since the transport scheme is switched on, ice has deformed after 144 time steps and is thicker and stronger, so that the convergence is more difficult.

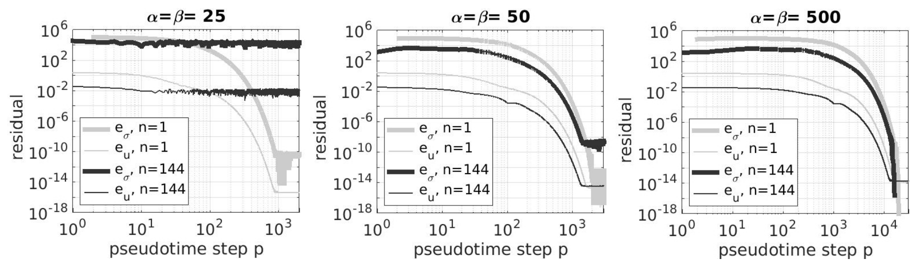

Figure 1: Global residuals e_σ and e_u for $\alpha = \beta \in \{25, 50, 500\}$ as a function of the pseudotime step. Results for $\alpha = \beta \in \{5000, 50000\}$ are similar to $\alpha = \beta = 500$ with larger N_c. The residual e_σ for $n = 1$ starts at iteration $p = 2$, as the initial value for $\boldsymbol{\sigma}$, in contrast to $\mathbf{u}$, has to be determined in the first subcycling step and is not given initially.

As discussed in Section 3 for the simplified 1D scheme, we expect low stability and consequently the loss of convergence for low α, for example for $\alpha = \beta = 5$. Further, for larger $\alpha = \beta = 25$ we reach convergence for the first time level, but do not at $n = 144$, which is already indicated by the noisy behaviour and relatively large magnitude of e_σ at the end of the first subcycling. The criterion $\gamma/(\alpha\beta) \ll 1$ can be violated for insufficiently high α, β, as the ice is in the viscous regime close to the wall and because a small Δ implies a large γ. Bearing this in mind and taking into account the magnitude of e_σ at the end of iterations at $n = 144$ we speculate that for the still moderate $\alpha = \beta = 50$, convergence may also be lost later after even thicker ice will have accumulated. The second and the third panels of Figure 1 reveal that the larger α and β, the better the convergence behaviour at the expense of an increasing N_c needed to reach it. According to Table 1, N_c increases linearly in α in agreement with our analysis of the simplified 1D scheme.

In the case of convergent subcycling, the initial residuals, i.e. $e_\sigma(1)$ and $e_u(1)$, are smaller after many time steps (Figure 1). However, the convergence of the EVP* solution is still exponential, as expected from the form of equations

(6) and (7). Note that the overall convergence is far too slow to be practical except for cases with moderate α, β.

We now relax the condition $\alpha = \beta$. Setting $\alpha < \beta$ means a stronger relaxation in the stress equations than in the momentum equation, and vice versa. The number of subcycling steps N_c that are necessary to reach convergence for our tests are given in Table 2. Comparing the pairs with the same product $\alpha\beta$ between Table 1 and Table 2 suggests that N_c is generally larger for $\alpha \neq \beta$ than for $\alpha = \beta$, consistent with the analysis in Section 3.

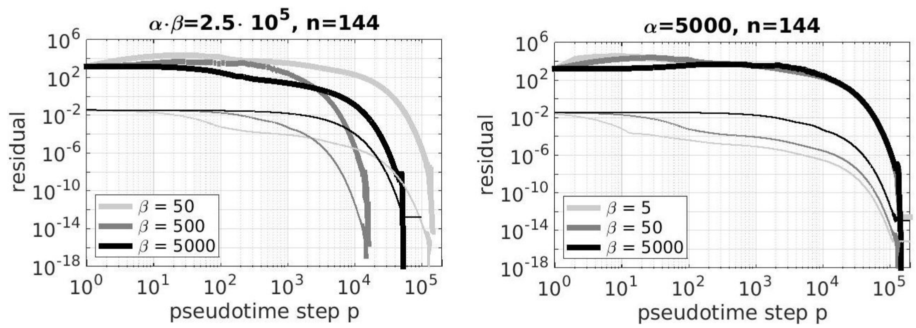

Figure 2: Residuals for (α, β) with $\alpha\beta = 2.5 \cdot 10^5$ (left), and $\alpha = 5000$ and $\beta \in \{5, 50, 5000\}$ (right) as a function of the pseudotime step at $n = 144$. For each color in one panel, thick lines of that color belong to e_σ and thin lines to e_u.

There is some asymmetry in the behaviour with respect to α and β (Table 2 and Figure 2) that cannot be explained by the analysis of Section 3. In particular, for fixed $\alpha\beta$ we get a faster convergence for $\alpha < \beta$ than for $\alpha > \beta$ (left hand side panel of Figure 2). Moreover, for $\beta \leq \alpha$ and α fixed, the convergence is still dictated by α and we find a value of N_c which coincides with that in

n \ $\alpha = \beta$	5	25	50	500	5000	$5 \cdot 10^4$
1	∞	950	1900	$1.9 \cdot 10^4$	$1.6 \cdot 10^5$	$1.4 \cdot 10^6$
144	∞	∞	1500	$1.5 \cdot 10^4$	$1.3 \cdot 10^5$	$1.2 \cdot 10^6$

Table 1: N_c for different choices of $\alpha = \beta$ at the first time level (first row) and at the 144th time level (second row). $N_c = \infty$ denotes a lack of convergence.

n \ $(\alpha,\, \beta)$	(5,500)	(500,5)	(50,5000)	(5000, 50)
1	8000	$1.8 \cdot 10^4$	$7.25 \cdot 10^4$	$1.75 \cdot 10^5$
144	6000	$1.5 \cdot 10^4$	$5.5 \cdot 10^4$	$1.4 \cdot 10^5$

Table 2: N_c for different choices of α and β at the first time level (first row) and at the 144th time level (second row).

simulations with $\alpha = \beta$ (right hand side panel of Figure 2). This behaviour is not observed for $\alpha \leq \beta$. This asymmetry shows the limitations of the *linear* analysis above (particularly, we neglected the strong nonlinearity in the stress equation) and stresses its qualitative character.

In summary, convergence is reached provided $\alpha\beta$ is sufficiently large and there is no advantage of selecting $\alpha \neq \beta$.

4.3. Impact of spatial resolution

We evaluate the impact of spatial resolution with four regular meshes of the given domain with resolutions $\Delta x \in \{0.05°,\ 0.1°,\ 0.5°,\ 1°\}$. In order to avoid the Courant stability criterion, we reduce the time step to $\Delta t = 180\,s$ and examine the iteration process of the first time level only. Figure 3 shows the convergence behaviour for the simulations with $\alpha = \beta \in \{100,\, 5000\}$. In order to consider the residuals independently of the number of degrees of freedom, we formulate them in root mean square sense. For $\alpha = \beta = 100$ (left panel of Figure 3) increasing the mesh resolution can lead to a loss of the convergence even at the first time level (see also Section 3). In our simulations there is no convergence if the resolution is finer than 0.1°. The convergence is recovered by increasing α and β, but still the residuals stagnate after 10^5 subcycles for the two finer meshes at some low level (right hand side panel of Figure 3). This happens despite the high values selected for α and β and rather small external time step. We did not explore the origin of this stagnation with high α as the reached degree of convergence is sufficient for most practical purposes.

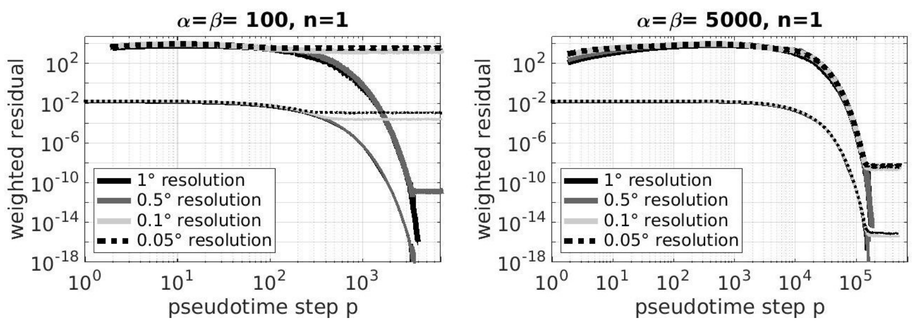

Figure 3: Weighted residuals for $\alpha = \beta = 100$ (left) and for $\alpha = \beta = 5000$ (right) as a function of the pseudotime step. The weighting is meant in the root mean square sense, that is $\widetilde{e}_\sigma = (e_\sigma^2/n_{cells})^{1/2}$ and $\widetilde{e}_u = (e_u^2/n_{nodes})^{1/2}$, n_{cells} and n_{nodes} denote the number of cells and nodes, respectively. For each color in one panel, thick lines of that color show $\widetilde{e}_\sigma$ and thin lines show $\widetilde{e}_u$.

4.4. "Practical" convergence for different $\alpha = \beta$

While large α and β are required for stability, a reduction by twelve orders of magnitude in the residuals at each time level is often neither required, nor practical. Instead, it is plausible to suppose that, provided that the last iterate of the previous time level is used as the initial guess for the current time level, sufficient accuracy can be reached across a sequence of time levels if the forcing changes slowly compared to the time step length. Here we illustrate the impact of choosing $N \ll N_c$ on a mesh with $\Delta x = 0.1°$, $\Delta t = 30$ min at $T = 30$ days ($n = 1440$). The reference solution is a VP solution obtained with the implicit VP solver of the sea ice model with 1000 Picard iterations at each time level. The corresponding solution components are shown in the upper four panels of Figure 4. Different EVP*-solutions are shown in the bottom four panels of the same figure.

In Figure 5, we present the residuals of EVP*-solutions at the last time level ($n = 1440$) for different $\alpha = \beta \in \{100, 250, 500\}$ and $N \in \{100, 500, 20000\}$. In Table 3 we summarize the deviations (errors) of the EVP*-solutions from the reference VP solution as l_2 norms. Strong ice is expected only where the concentration is close to one. Therefore we restrict the l_2-norms to regions with $a_{vp} > 0.9$. For $\alpha = \beta = 100$ the errors are independent of N and there is no convergence, consistent with noisy divergence and Δ fields in Figure 4 (third row). These errors are at least one order of magnitude larger than for the remaining cases. For $\alpha = \beta = 250$, the errors are reduced in going from $N = 100$ to $N = 500$, but remain (nearly) the same with an even increased $N = 20,000$. The still insufficient magnitudes of α and β are also reflected in some small-amplitude noise in the fields of divergence and Δ. The noise is too small to be visible in Figure 4 (bottom row), but can be recognized in the deviations from the reference solution in Figure 6 (top row). For $\alpha = \beta = 500$, the solutions converge (Figure 5) and hence the errors decrease with increased N (Table 3). In contrast to the case $\alpha = \beta = 250$ (Figure 6 (top row)) we do no longer observe noise in the solution (Figure 6 (bottom row)).

In Figure 6, we observe for increasing N that the solution for $\alpha = \beta = 250$ is unstable in the south-east corner where $\Delta \sim \Delta_{\min}$, but it converges faster than the formally more stable solution of $\alpha = \beta = 500$. This behaviour illustrates how the convergence of the EVP* scheme is controlled by $1/\alpha$ and $1/\beta$: large values of α and β lead to stable but slowly converging solutions, whereas small values of α and β lead to faster convergence in the case of weak stability requirements.

To explore the behaviour of the scheme in the regime with fewer subcycles in greater detail, we compare partially converged EVP*-solutions to the reference solution for the divergence field and the ice concentration a in Figure 6 and Figure 7 respectively. The behaviour of h and Δ leads to similar conclusions (not shown). According to Table 3, changing α (and β) from 100 to 250 reduces the already small mean error by one order of magnitude. The remaining errors in concentration a are found near the ice edge (because of large spatial gradients in concentration) and in the bottom right corner of the domain (top row of Figures 7). Increasing N reduces the residual errors near the ice edge, but cannot remove the error in the lower right corner. Apparently, EVP* does not converge to the reference VP-solution in this area, but note that the differences to the reference solution are very small (order 10^{-3} or 0.1% ice cover). Increasing α to 500 (bottom row of Figure 7) slows down the convergence (due to the smaller

$\alpha = \beta$	N	$\|\|e_a\|\|$	$\|\|e_h\|\|$	$\|\|\mathbf{e}_{vel}\|\|$	$\|\|e_{div}\|\|$	$\|\|e_\Delta\|\|$
100	100	$7.0 \cdot 10^{-3}$	$3.0 \cdot 10^{-2}$	$5.2 \cdot 10^{-3}$	$1.2 \cdot 10^{-7}$	$6.8 \cdot 10^{-8}$
100	500	$7.0 \cdot 10^{-3}$	$3.0 \cdot 10^{-2}$	$5.0 \cdot 10^{-3}$	$1.2 \cdot 10^{-7}$	$6.8 \cdot 10^{-8}$
100	20000	$7.0 \cdot 10^{-3}$	$3.0 \cdot 10^{-2}$	$5.0 \cdot 10^{-3}$	$1.1 \cdot 10^{-7}$	$6.7 \cdot 10^{-8}$
250	100	$9.7 \cdot 10^{-4}$	$2.2 \cdot 10^{-3}$	$3.9 \cdot 10^{-4}$	$1.2 \cdot 10^{-8}$	$4.1 \cdot 10^{-9}$
250	500	$4.9 \cdot 10^{-4}$	$1.2 \cdot 10^{-3}$	$1.2 \cdot 10^{-4}$	$3.1 \cdot 10^{-9}$	$1.3 \cdot 10^{-9}$
250	20000	$4.7 \cdot 10^{-4}$	$1.2 \cdot 10^{-3}$	$9.3 \cdot 10^{-5}$	$2.4 \cdot 10^{-9}$	$1.3 \cdot 10^{-9}$
500	100	$1.5 \cdot 10^{-3}$	$4.0 \cdot 10^{-3}$	$6.2 \cdot 10^{-4}$	$2.2 \cdot 10^{-8}$	$7.8 \cdot 10^{-9}$
500	500	$3.4 \cdot 10^{-4}$	$9.0 \cdot 10^{-4}$	$2.6 \cdot 10^{-4}$	$6.3 \cdot 10^{-9}$	$1.5 \cdot 10^{-9}$
500	20000	$1.4 \cdot 10^{-4}$	$7.5 \cdot 10^{-4}$	$4.9 \cdot 10^{-5}$	$2.1 \cdot 10^{-9}$	$6.1 \cdot 10^{-10}$

Table 3: Mean deviations of the EVP* solutions from the VP reference solution with 1000 Picard iterations at day 30 after subcycling with N subcycling steps. The error for the mean thickness is measured as $||e_h||^2 := \sum_i (h_{evp,i} - h_{vp,i})^2/n_n$ with summation over the nodes where $a_{vp} > 0.9$ and n_n the number of such nodes, same for the concentration and velocity; for the divergence and Δ summation is over elements and errors are per element.

correction parameters α^{-1} and β^{-1}), so that for $N = 100$ and 500 some of the errors are even a bit larger than for $\alpha = 250$, but the largest differences in the bottom right corner are removed and EVP* converges to the reference solution.

Note that the solutions for the ice concentration a and thickness h appear smooth even for $\alpha = 100$ (not shown), but the convergence is poor. The divergence fields, however, (and similarly Δ), are very noisy for $\alpha \leq 250$ and this noise cannot be removed with more subcycles (top row of Figure 6). In fact, the noise is most likely responsible for the loss of convergence. Increasing α to 500 leads to smooth divergence fields even for small N. The errors in the divergence fields decrease with larger N (bottom row of Figure 6).

Figures 6 and 7 illustrate that acceptable EVP*-solutions can be obtained for a moderate number of subcycles $N < N_c$. The value of α (and β) determines the stability and hence smoothness of the solution. Once α and β are sufficiently high to guarantee stability, the convergence is strictly exponential, so that larger N lead to more accurate (albeit more expensive) solutions.

Finally, we consider states of stress of the EVP* and reference VP solutions plotted in Fig. 8. The black and grey dots in the plots relate to the regions where $a < 0.7$ and $a \geq 0.7$ respectively. For the reference solution (the bottom panel) the stresses are either on the elliptic yield curve, or correspond to points inside it, as expected for the VP rheology. For the EVP* solutions the stresses tend to the VP behaviour with increasing α and β, in agreement with the convergence behaviour seen in Figure 5. The distribution of the black dots in the first column of Figure 8 for $N = 100$ illustrates the reduction of the convergence rate with increasing parameters α and β for fixed N. These dots correspond to weak ice that is more sensitive to the details of convergence because it continues to move under variable winds. With $\alpha = \beta = 250$ and N sufficiently large ($N = 500$), most of the states of stress are either inside or on the yield curve.

Thus, once again, the improvement in the EVP* solutions is gained by increasing the parameters α and β. Once they are sufficiently large, increasing N further improves the quality of the EVP* solution. However, the larger α and β, the slower is the convergence of the entire system.

5. Conclusions

Our analysis of the EVP* scheme [5, 11] clarifies some aspects that have not been addressed in [11]. We derived the formal stability condition $\gamma/\alpha\beta < 4$. However, this is associated with oscillations. The stability condition of [11], $\gamma/\alpha\beta \leq 2$, only ensures that the absolute value of the frequency is less than $\pi/2$, which implies two iterations before the change in sign. As nonlinearity is an intrinsic part of the EVP* equations, the much stronger condition $\gamma/\alpha\beta \ll 1$ needs to be ensured, such that the oscillations, that develop in the system, are of low frequency and are therefore resolved by the pseudotime stepping. In contrast to [11], we show that the roles of α and β are similar. The choice $\alpha = \beta$ is most convincing, because otherwise there are two convergence rates in regions with weak ice, one set by α and the other one by β. Additionally, in two dimensions the velocity vector $\mathbf{u}$ is not necessarily aligned with the stress divergence vector $\nabla \cdot \boldsymbol{\sigma}$ and the component perpendicular to $\nabla \cdot \boldsymbol{\sigma}$ will thus tend to converge at a rate defined by β. Hence, the parameters α and β should be sufficiently large and sufficiently similar.

Our analysis as well as the experiments show that the larger α and β, the larger is the number N_c of iterations needed to reach convergence on each time level. In practice, iterations with N_c cycles are too expensive, and a compromise between stability and accuracy has to be found. The link between N_c, α and β was already apparent in the experiments of [11], where either N was far too small to reach convergence for large α and β, or the product $\alpha\beta$ was too small to ensure stability.

Ice concentration a and thickness h are affected less severely by incomplete convergence and instabilities than the divergence and Δ. The EVP* solutions for a and h were smooth and rather close to the VP reference solution in our simulations even for values of α, β and N that were too small to satisfy stability and convergence criteria, but derivatives of the velocity field suffered from noise unless α and β were sufficiently large. Only in the case when stability is reached, increasing N improves the accuracy of velocity derivatives.

Refining the mesh makes the EVP* scheme less stable and may require increased α and β, which in turn would lead to slower convergence.

We stress once again the qualitative character of our analysis. However, it illustrates that the EVP* scheme can converge to the VP solution, even if achieving full convergence may prove difficult. While in practice uncertainties (e.g., in forcing) may lead to errors that by far exceed the errors due to incomplete convergence of the EVP* scheme, it is important to be aware of the effects of the method parameters on the solution.

The method can be extended to include variable parameters α and β. They may depend on spatial coordinates in order either to improve convergence or preserve stability or both or they can depend on the convergence rate itself: small values of α and β lead to fast convergence in the beginning and larger values damp instability later in the interaction. These extensions and their evaluation are left to future work.

[1] W. D. Hibler III, A Dynamic Thermodynamic Sea Ice Model, J. Phys. Oceanogr. 9 (1979) 815–846. doi:http://dx.doi.org/10.1175/1520-0485(1979)009<0815:ADTSIM>2.0.CO;2.

[2] J. Zhang, W. Hibler, On an efficient numerical method for modeling sea ice dynamics, J. Geophys. Res. 102 (C4) (1997) 8691–8702. doi:10.1029/96JC03744.

[3] J.-F. Lemieux, B. Tremblay, Numerical convergence of viscous–plastic sea ice models, J. Geophys. Res. 114 (C5). doi:10.1029/2008JC005017.

[4] J.-F. Lemieux, B. Tremblay, J. Sedlacek, P. Tupper, S. Thomas, D. Huard, J.-P. Auclair, Improving the numerical convergence of viscous–plastic sea ice models with the Jacobian–free Newton–Krylov method, J. Comp. Phys. 229 (8) (2010) 2840–2852. doi:http://dx.doi.org/10.1016/j.jcp.2009.12.011.

[5] J.-F. Lemieux, D. Knoll, B. Tremblay, D. Holland, M. Losch, A comparison of the Jacobian–free Newton–Krylov method and the EVP model for solving the sea ice momentum equation with a viscous–plastic formulation: a serial algorithm study, J. Comp. Phys. 231 (2012) 5926–5944. doi:10.1016/j.jcp.2012.05.024.

[6] M. Losch, A. Fuchs, J.-F. Lemieux, A. Vanselow, A parallel Jacobian–free Newton–Krylov solver for a coupled sea ice–ocean model, J. Comp. Phys. 257, Part A (0) (2014) 901–911. doi:10.1016/j.jcp.2013.09.026.

[7] E. Hunke, J. Dukowicz, An Elastic-Viscous-Plastic model for sea ice dynamics, J. Phys. Oceanogr. 27 (1997) 1849–1867. doi:http://dx.doi.org/10.1175/1520-0485(1997)027<1849:AEVPMF>2.0.CO;2.

[8] E. Hunke, Viscous-plastic sea ice dynamics with the EVP model: Linearization issues, J. Comp. Phys. 170 (1) (2001) 18–38. doi:http://dx.doi.org/10.1006/jcph.2001.6710.

[9] M. Losch, D. Menemenlis, J.-M. Campin, P. Heimbach, C. Hill, On the formulation of sea–ice models. Part 1: Effects of different solver implementations and parameterizations, Ocean Modelling 33 (12) (2009) 129–144. doi:http://dx.doi.org/10.1016/j.ocemod.2009.12.008.

[10] M. Losch, S. Danilov, On solving the momentum equations of dynamic sea ice models with implicit solvers and the elastic–viscous–plastic technique, Ocean Modelling 41 (0) (2012) 42–52. doi:http://dx.doi.org/10.1016/j.ocemod.2011.10.002.

[11] S. Bouillon, T. Fichefet, V. Legat, G. Madec, The elastic-viscous-plastic method revisited, Ocean Modelling 71 71 (0) (2013) 2–12. doi:http://dx.doi.org/10.1016/j.ocemod.2013.05.013.

[12] S. Danilov, Q. Wang, R. Timmermann, N. Iakovlev, D. Sidorenko, M. Kimmritz, T. Jung, J. Schröter, Finite-Element Sea Ice Model (FESIM), version 2, Geoscientific Model Development Discussions 8 (2) (2015) 855–896. doi:10.5194/gmdd-8-855-2015.

[13] Q. Wang, S. Danilov, D. Sidorenko, R. Timmermann, C. Wekerle, X. Wang, T. Jung, J. Schröter, The Finite Element Sea Ice–Ocean Model (FESOM) v.1.4: formulation of an ocean general circulation model, Geoscientific Model Development 7 (2) (2014) 663–693. doi:10.5194/gmd-7-663-2014.

[14] W. D. Hibler III, C. F. Ip, The effect of sea ice rheology on Arctic buoy drift, J. P. Dempsey and Y. D. S. Rajapakse (eds.) ASME AMD 207, Ice Mechanics (1995) 255–263.

[15] E. Hunke, W. Lipscomb, CICE: The Los Alamos sea ice model documentation and software users manual, Tech. rep., T-3 Fluid Dynamics Group, Los Alamos National Laboratory, Los Alamos NM 87545 (2008).

[16] R. Timmermann, S. Danilov, J. Schröter, C. Böning, D. Sidorenko, K. Rollenhagen, Ocean circulation and sea ice distribution in a finite element global sea ice–ocean model, Ocean Modelling 27 (3–4) (2009) 114–129.

[17] R. Löhner, K. Morgan, J. Peraire, M. Vahdati, Finite–element flux–corrected transport (FEM–FCT) for the Euler and Navier–Stokes equations, Internat. J. Numer. Meth. Fluids 7 (10) (1987) 1093–1109. doi:10.1002/fld.1650071007.

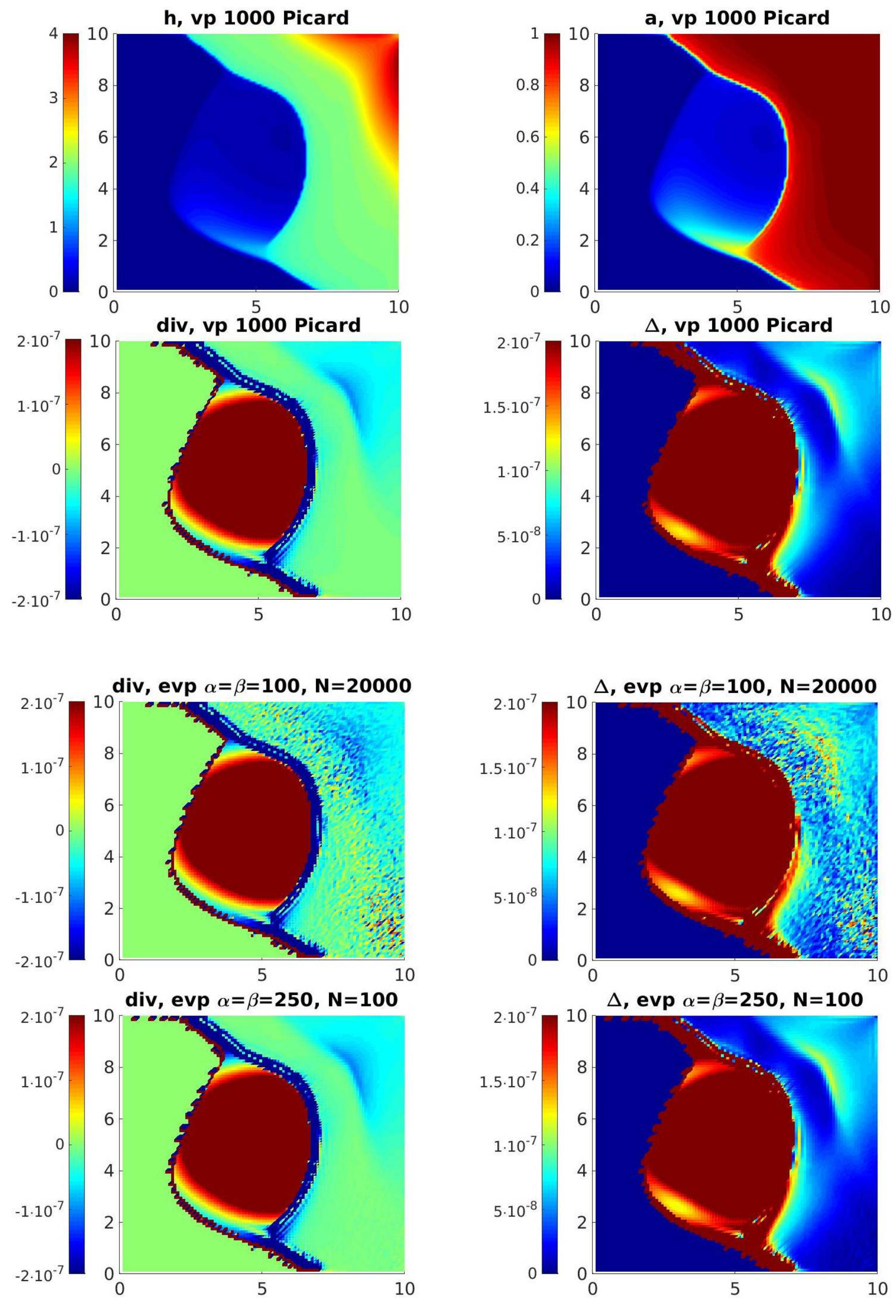

Figure 4: Upper four panels: the mean ice thickness, concentration, divergence and the field of Δ for the reference solution (VP solver with 1000 Picard iterations) after 30 days ($n = 1440$). Lower four panels: Patterns of divergence (left) and Δ_{evp} (right) for $\alpha = \beta = 100$ and $N = 20,000$ (third row) and for $\alpha = \beta = 250$ and $N = 100$ (fourth row).

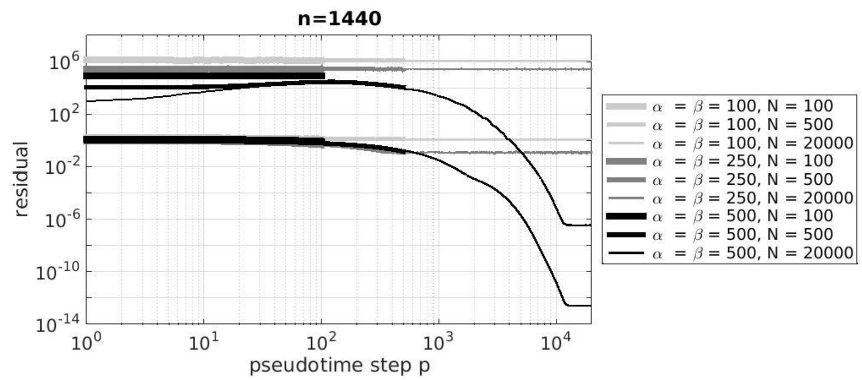

Figure 5: The behaviour of e_σ and e_u as a function of pseudotime step for different values of $\alpha = \beta$ and N at time level $n = 1440$ (30 days).

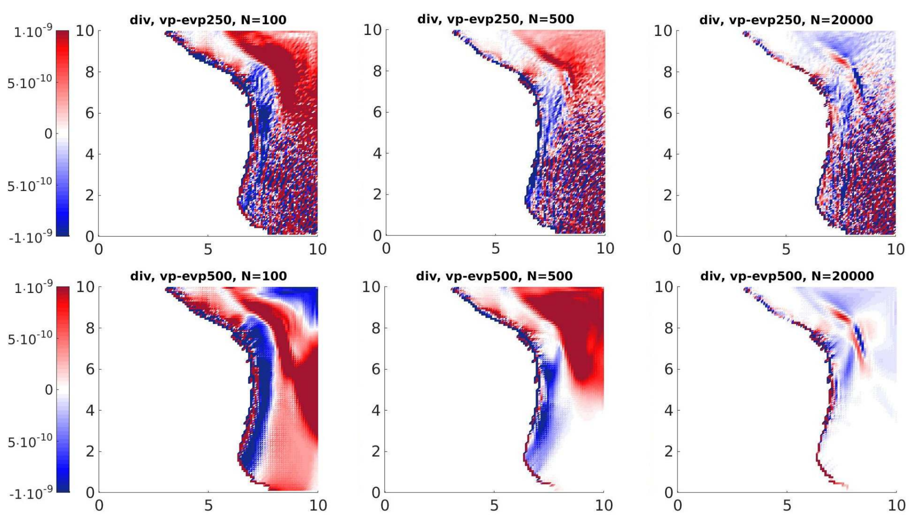

Figure 6: Differences in the divergence field $\nabla \cdot \mathbf{u}$ where $a > 0.9$ between selected EVP*-solutions and the reference VP solution. $\alpha = \beta = 250$ (top row) are sufficient to maintain stability over the northern part of the domain. The increase in N reduces the error there, but does not help over the southern part. Larger α, β handle this issue (bottom row).

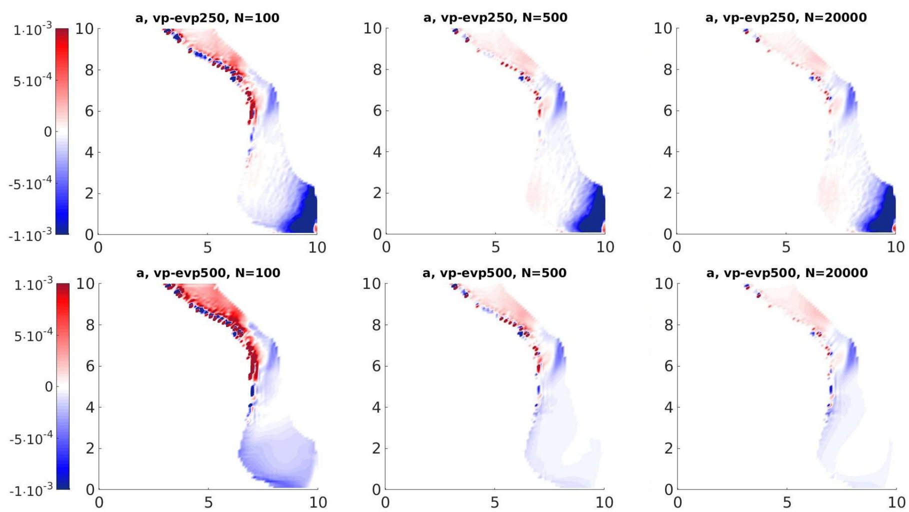

Figure 7: Differences in the ice concentration a for $a > 0.9$ between selected EVP*-solutions and the reference VP solution. The EVP*-solutions are for $\alpha = \beta = 250$ (top row) and for $\alpha = \beta = 500$ (bottom row) for different $N \in \{100, 500, 20000\}$ (from left to right). Small differences in the southeast corner can only be removed by using larger α.

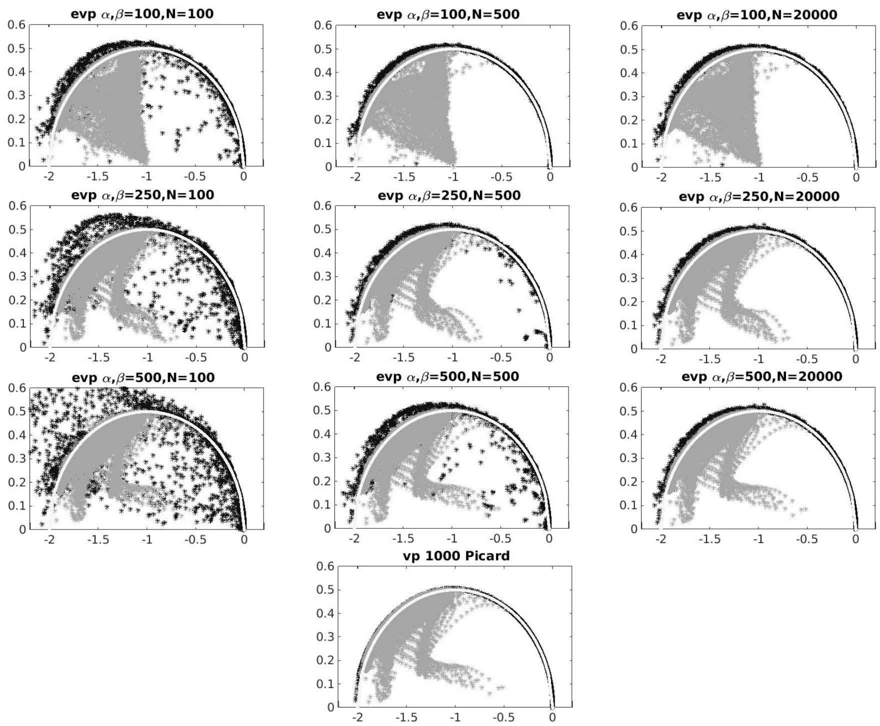

Figure 8: Normalized states of stress for different EVP* solutions (three rows) and for the reference VP solution (bottom panel). The black (grey) dots correspond to regions where $a < 0.7(\geq 0.7)$. The light grey curve plots the ideal elliptic curve. For high α and N the EVP* state of stress is rather close to that of reference VP solution. Insufficiently high α result in different pattern of grey dots (top row), but insufficiently high N for larger α emphasizes the contribution of pseudotime terms for weak ice.